https://doi.org/10.5194/egusphere-2023-1947
Preprint. Discussion started: 13 September 2023

A rigorous approach to the specific surface area evolution in snow during temperature gradient metamorphism

Anna Braun[1,2], Kévin Fourteau[1], and Henning Löwe[1]

[1]Group Snow Physics, Research Unit Snow and Atmosphere, WSL Institute for Snow and Avalanche Research SLF, 7260 Davos Dorf, Switzerland
[2]Laboratory of Cryospheric Sciences, School of Architecture, Civil and Environmental Engineering, Ecole Polytechnique Federale de Lausanne, 1015 Lausanne, Switzerland

Correspondence: Henning Löwe (loewe@slf.ch)

Abstract. Despite being one of the most fundamental microstructural parameters of snow, the specific surface area (SSA) dynamics during temperature gradient metamorphism (TGM) have so far been addressed only within empirical modeling. To surpass this limitation, we propose a rigorous modeling of SSA dynamics using an exact equation for the temporal evolution of the surface area, fed by pore-scale finite element simulations of the water vapor field coupled with the temperature field on X-ray computed-tomography images. The proposed methodology derives from physics' first principles and thus does not rely on any empirical parameter. Since the calculated evolution of the SSA is highly sensitive to fluctuations in the experimental data, we address the impact of these fluctuations within a stochastic error model. In our simulations, the only poorly constrained physical parameter is the vapor attachment coefficient α onto ice. We address this problem by simulating the SSA evolution for a wide range of α and estimate optimal values by minimizing the differences between simulations and experiments. This methodology suggests that α lies in the intermediate range $10^{-3} < \alpha < 10^{-1}$ and slightly varies between experiments. Also, our results suggest a transition of the value of α in one TGM experiment, which can be explained by a transition in the underlying surface morphology. Overall, we are able to reproduce very subtle variations in the SSA evolution with correlations of $R^2 = 0.95$ and 0.99, respectively, for the two considered TGM time series. Finally, our work highlights the necessity of including kinetics effects and of using realistic microstructures to comprehend the evolution of SSA during TGM.

1 Introduction

The specific surface area (SSA) of snow is the interface area between ice and air in the microstructure of porous snow that determines many structural and physical properties of the snow cover. The SSA is a crucial parameter for the optical albedo of snow (Dumont et al., 2014), fluid permeability (Zermatten et al., 2014), avalanche prediction (Schweizer et al., 2003), microwave remote sensing (Picard et al., 2022), or chemical exchange with the atmosphere (Hanot and Dominé, 1999). The SSA evolution in time is the key to quantifying metamorphism (Legagneux et al., 2004; Domine et al., 2006; Pinzer et al., 2012; Wang and Baker, 2014; Harris Stuart et al., 2023) and needs to be faithfully parameterized in snow cover models to capture the evolution of physical properties. Temperature gradient metamorphism (TGM) is by far the most important type of metamorphism in dry, natural snow covers (Schneebeli and Sokratov, 2004; Legagneux et al., 2004), since gradient-free

https://doi.org/10.5194/egusphere-2023-1947
Preprint. Discussion started: 13 September 2023

(i.e., isothermal) conditions exist at most in deep polar firn. However, a detailed physical understanding of the SSA evolution under TGM is still lacking.

Detailed experimental data on TGM can be conveniently acquired nowadays through X-ray micro-computed tomography (μCT). Imaging of snow samples with μCT was developed over the last two decades (Coleou et al., 2001; Flin et al., 2004; Schneebeli and Sokratov, 2004; Schleef and Loewe, 2013) and provides 3D insight into the microstructure that is otherwise invisible to the naked eye. In contrast to many destructive snow measurement methods, μCT preserves the structure of the snow. Since the entire snow microstructure is available, any parameter of interest, especially SSA, can be computed within established uncertainties due to reconstruction and image analysis (Hagenmuller et al., 2016). By using instrumented sample holders to constrain temperatures and temperature gradients, in-situ time-lapse observations of the microstructure during TGM are obtained (Kaempfer et al., 2005; Pinzer et al., 2012; Calonne et al., 2014a; Hammonds et al., 2015; Wiese and Schneebeli, 2017; Li and Baker, 2022). While many SSA evolution curves originated from these studies, none of them has been convincingly reproduced from a physical model.

Physical models of snow metamorphism must comply with the ice crystal growth dynamics at the pore scale (Krol and Löwe, 2016), which comprises vapor and heat diffusion, accommodated by attachment kinetics controlling the deposition and sublimation of water molecules onto the ice lattice (Colbeck, 1983; Libbrecht, 2005). The key parameter in this picture is the vapor attachment coefficient α that controls the kinetics of vapor deposition and sublimation. The kinetic parameter is applicable at the micro-meter scale of ambient diffusion processes and thereby subsumes the underlying nano-scale kinetics resulting from the molecular dynamics on the surface of the ice crystal lattice (Saito, 1996). Many measurement and modeling attempts carefully characterize α for ice crystals (Libbrecht, 2005; Hobbs, 2010; Barrett et al., 2012; Libbrecht and Rickerby, 2013; Pokrifka et al., 2020). Nevertheless, α is experimentally challenging to constrain even for isolated crystal growth. One reason is the fundamental, experimental difficulty of inverting growth data as soon as diffusion is involved (Libbrecht, 2005). The other reason is that α depends on numerous effects such as temperature, supersaturation, and crystallographic orientation (Saito, 1996; Libbrecht, 2005). The large variations between basal and prismatic surface kinetics are, for example, the key to snow crystal morphology (Barrett et al., 2012). The situation is even more complicated in the snow cover where many different surface orientations exist simultaneously (Granger et al., 2021). Therefore, the kinetics is more difficult to assess in snow, and only a few studies exist constraining α from the comparison of μCT-based simulations with experiments (Bouvet et al., 2022; Fourteau et al., 2021a). Thus, α constitutes the great unknown in snow metamorphism as commonly stressed in TGM models (Miller and Adams, 2009; Kaempfer and Plapp, 2009; Calonne et al., 2014b).

Model attempts characterizing TGM can be classified by their treatment of attachment kinetics and whether the microstructure is taken from μCT or geometrically idealized. Using μCT images, (Flin and Brzoska, 2008) calculated deposition fluxes in the absence of kinetics under the assumption of local equilibrium at the interface (diffusion-limited growth). A similar approximation was used in (Krol and Löwe, 2016) to relate the temperature gradient driven deposition fluxes to measured, local growth velocities. The latter can be considered as a generalization of the (diffusion-limited) air bubble migration under a temperature gradient in ice (Shreve, 1967) to complex geometries. However, the assumption of purely diffusion-limited growth was already questioned (Krol and Löwe, 2018) due to contradictions with the measured SSA evolution. The μCT-based theoretical ho-

https://doi.org/10.5194/egusphere-2023-1947
Preprint. Discussion started: 13 September 2023

mogenization (Calonne et al., 2014b), in contrast, applies to the slow kinetics (i.e., kinetics-limited) regime. The intermediate regime from diffusion to kinetics vapor transport under a temperature gradient was numerically analyzed in (Fourteau et al., 2021a), where the latter approach is physically similar to the phase field model (Kaempfer and Plapp, 2009). Common to all μCT-based approaches is that the choice of α has a significant impact on numerical effort. It is therefore not surprising that the majority of modeling attempts exist for simplified geometries (mostly spheres) (Adams and Brown, 1982; Colbeck, 1983; Albert and McGilvary, 1992; Miller and Adams, 2009), at the downside of microstructural realism. The most widely used models for predicting the SSA evolution under TGM are those implemented in detailed snow cover models e.g., (Flanner and Zender, 2006). Like other simplified models, (Flanner and Zender, 2006) neglect kinetics and employ diffusion-limited growth for distribution of spherical particles. Due to the involved empirical parameters (mean sphere radius and spacing), which prevent an unambiguous mapping onto arbitrary microstructures, validating these models through μCT laboratory experiments would remain inconclusive.

In principle, no empiricism is required, and the SSA evolution for arbitrary 3D microstructure can be computed exactly (Krol and Löwe, 2018), as long as the required parameters are supplied. The surface area equation is rigorously formulated in terms of a rate term that can be computed from the interfacial curvature and the interface growth velocity $v_\mathbf{n}$ after volume averaging. While the first is a geometrical quantity, the second must be computed from a physical model. Any model that predicts $v_\mathbf{n}$ as the result of 3D heat and mass diffusion with interface kinetics could be employed here, either phase field models (Kaempfer and Plapp, 2009) or diffusion models (Fourteau et al., 2021b). Both are equivalent in view of the involved physics and only differ in their representation of the interface. This route to the SSA evolution in TGM is rigorous (apart from numerical approximations) but has never been pursued before. Advancing on this route is the aim of the present work. To this end, we combine a finite element (FE) solution of the pore-scale vapor and heat diffusion equations following (Fourteau et al., 2021b) with the exact surface area equation from (Krol and Löwe, 2018) in order to reproduce the SSA evolution during TGM from the four-dimensional (4D) μCT image data from (Pinzer et al., 2012).

The manuscript is organized as follows. The theoretical background for pore-scale diffusion and the SSA is presented in Sect. 2. In Sect. 3, we describe the numerical procedures (meshing, FE solution, image processing), a simple stochastic error analysis, and the validation of our numerical workflow against an analytical solution. The simulations for the TGM time series are shown in Sect. 4 and discussed in Sect. 5.

2 Theoretical background

2.1 Heat and vapor transfer at the pore scale

For an arbitrary snow structure, morphological changes during metamorphism are driven by the coupled diffusion of heat and mass together with ice-air interface motion due to deposition and sublimation. In the following, we closely follow the descriptions by (Kaempfer and Plapp, 2009; Calonne et al., 2014b; Krol and Löwe, 2016; Fourteau et al., 2021a). We consider a representative snow volume at the micro-scale consisting of ice and air and denote the sub-domains occupied by the solid and air phase by Ω_i and Ω_a, respectively. In the following subscripts i and a denote quantities which are defined in the respective

https://doi.org/10.5194/egusphere-2023-1947
Preprint. Discussion started: 13 September 2023

domains Ω_i and Ω_a. Due to the separation of time scales between the diffusion of heat and mass in the pores and the motion of the interface due to crystal growth, we employ the common assumption of small particle Peclet numbers (Libbrecht, 2005) and consider stationary diffusion equations for heat and mass. Accordingly, the partial density of water vapor in air ρ_v and the ice and air temperatures T_i and T_a, respectively, are governed by

$$D_v \nabla^2 \rho_v = 0 \qquad \text{in } \Omega_a \tag{1}$$

$$\kappa_a \nabla^2 T_a = 0 \qquad \text{in } \Omega_a \tag{2}$$

$$\kappa_i \nabla^2 T_i = 0 \qquad \text{in } \Omega_i \tag{3}$$

where D_v is the vapor diffusion constant in air, κ_i and κ_a are the thermal diffusivities of ice and air, respectively.

The diffusion equations are coupled via boundary conditions on the ice-air interface Γ. The mass conservation at the ice-air interface is linked to the water vapor concentration by a Stefan-type condition

$$(\rho_i - \rho_v)\, v_{\mathbf{n}} \;=\; D_v\, \mathbf{n} \cdot \nabla \rho_v \qquad \text{on } \Gamma \tag{4}$$

where ρ_i denotes the ice density and $\mathbf{n}$ the unit normal vector field on Γ which is oriented into the pore space Ω_a and $v_{\mathbf{n}}$ is the growth velocity on Γ in the direction of $\mathbf{n}$. The velocity $v_{\mathbf{n}}$ is therefore positive for deposition and negative for sublimation.

The conservation of energy requires the continuity of temperature and heat flux on the ice-air interface according to

$$T_i \;=\; T_a \qquad \text{on } \Gamma \tag{5}$$

$$\kappa_i\, \mathbf{n} \cdot \nabla T_i \;=\; \kappa_a\, \mathbf{n} \cdot \nabla T_a \qquad \text{on } \Gamma \tag{6}$$

As in (Krol and Löwe, 2016), the latent heat during the sublimation and deposition is neglected. Since mass and energy conservation involves the unknown interface velocity $v_{\mathbf{n}}$, the internal boundary conditions must be completed by a constitutive law that characterizes $v_{\mathbf{n}}$ during crystal growth. Here, we employ the Hertz-Knudsen law (Libbrecht, 2005; Kaempfer and Plapp, 2009; Fourteau et al., 2021a), which includes the impact of interfacial curvature on the equilibrium vapor concentration (Gibbs-Thomson effect) according to

$$\rho_v = \rho_{v,s}(T)(1 + d_0\, H) + \frac{\rho_i}{\alpha\, v_{\mathrm{kin}}} v_{\mathbf{n}} \qquad \text{on } \Gamma \tag{7}$$

The equilibrium (or saturation) vapor concentration on a flat surface at temperature T is denoted by $\rho_{v,s}(T)$, the capillary length by d_0, the mean curvature by H, the condensation coefficient by α and the kinetic velocity by v_{kin}. The capillary length is related to $d_0 = \gamma\, a^3/(k_B\, T)$, where γ is the interfacial free energy, a is the mean intermolecular spacing of water molecules in ice and k_B is the Boltzmann constant. The kinetic velocity is defined here as $v_{\mathrm{kin}} = \sqrt{k_B\, T/(2\,\pi\, m)}$ with the mass of water molecule m. This definition follows (Fourteau et al., 2021a) and thus differs from the definition in (Libbrecht, 2005). In the Hertz-Knudsen equation, the kinetic coefficient α has the meaning of a sticking probability of water molecules impinging onto the surface. Therefore, values in the range $[0, 1]$ are commonly desired, where $\alpha \to 0$ corresponds to slow surface kinetics and for $\alpha \approx 1$ the diffusion dominated regime will be attained (Libbrecht, 2005; Fourteau et al., 2021a). Mathematically the equation remains well-defined also for $\alpha > 1$, which may be physically interpreted as deviations from the local constitutive behavior (7) due to non-local surface processes (Libbrecht, 2005).

https://doi.org/10.5194/egusphere-2023-1947
Preprint. Discussion started: 13 September 2023

2.2 Evolution of SSA

The solution of the diffusion system (Eq. (1)-(3)) with boundary conditions (Eq. (4)-(7)) yields the spatially varying growth velocity $v_{\mathbf{n}}$ at any point on the ice-air interface Γ. As shown by (Drew, 1990; Krol and Löwe, 2018), this information is sufficient to calculate the evolution of the SSA rigorously via volume averaging. As a result, for single grains or statistically homogeneous microstructures, the equation for specific surface area (per unit volume) s can be expressed as follows:

$$\dot{s} = 2\, s\, \overline{v_{\mathbf{n}} H} \tag{8}$$

Here the rate term $\overline{v_{\mathbf{n}} H}$ is the product of local interface velocity $v_{\mathbf{n}}$ and the local mean curvature H averaged over the ice-air interface area. Equation (8) is a linear homogeneous first-order ordinary differential equation and can be formally solved in closed form by separation of variables yielding

$$s(t) = s(0)\, \exp\left(2 \int_0^t \overline{v_{\mathbf{n}} H}(\tau) d\tau \right) \tag{9}$$

The representation Eq. (9) allows us to compute the SSA evolution from the rate term $\overline{v_{\mathbf{n}} H}$ which must be computed from the solution of the 3D diffusion problem. This link between the SSA evolution and the heat and mass diffusion equations is rigorous. The closely related specific surface area (per ice volume) SSA_V can then be computed as

$$SSA_V = \frac{s}{\phi_i} \tag{10}$$

in terms of the ice volume fraction ϕ_i. The quantity SSA_V is more commonly used in the snow community (e.g., Matzl and Schneebeli, 2006) since it directly defines the optical diameter.

3 Numerical modeling

3.1 Micro tomography time lapse experiments

The numerical simulations were conducted on 4D image data of two TGM experiments (Series 1 and 2), which were previously acquired and already analyzed in (Pinzer et al., 2012) and (Krol and Löwe, 2016). In the experiments, a constant temperature gradient was applied by adjusting a snow samples's bottom and top temperature in an instrumented tomography sample holder, known as Snowbreeder (Pinzer and Schneebeli, 2009a). Series 1 lasted 384 h and is shorter than Series 2, which lasted 665 h. The mean temperature T and the temperature gradient ∇T are similar for the both series: T = -8.1 °C, ∇T = 47 Km^{-1} for Series 1 and T = -7.6 °C, ∇T = 55 Km^{-1} for Series 2. Both time series start from rounded grains with slightly different initial values of SSA and volumetric density, namely $SSA_V(t=0) = 20\ \mathrm{mm}^{-1}$, $\phi_i(t=0) = 0.31$ for Series 1 and $SSA_V(t=0) = 24\ \mathrm{mm}^{-1}$, $\phi_i(t=0) = 0.28$ for Series 2. For further experimental details, we refer to (Pinzer et al., 2012).

https://doi.org/10.5194/egusphere-2023-1947
Preprint. Discussion started: 13 September 2023

The X-ray micro-computed tomography image data were extracted from the snow sample every eight hours in time-lapse mode and segmented into binary images as described previously (Pinzer et al., 2012). These binary images are denoted by

$$I(t_n), \quad n = 1, 2, \ldots, 49 \qquad \text{for Series 1} \tag{11}$$

$$\tilde{I}(t_m), \quad m = 1, 2, \ldots, 84 \qquad \text{for Series 2} \tag{12}$$

at different time steps and are $300 \times 300 \times 196$ voxel images with voxel size $25 \cdot 10^{-6}$ m in Series 1 and $18 \cdot 10^{-6}$ m in Series 2. Both series show the commonly observed decay of SSA (Taillandier et al., 2007; Pinzer and Schneebeli, 2009b; Calonne et al., 2014a).

3.2 FE solution of temperature and vapor fields

3.2.1 Meshing

An appropriate mesh that preserves the ice-air interface and produces a reasonable volumetric division is a key requirement for an accurate numerical solution to the problem. To this end, we employ the open-source Computational Geometry Algorithms Library (CGAL) (The CGAL Project, 2022) and use the `Polyhedral_mesh_domain_with_features_3` class that implements volume meshing of a domain that is bounded by a polyhedral surface which is preserved. The surface needs to be closed and free of intersections. To obtain such a closed surface, we extract the ice-air interface from the binary μCT data (Eq. (11) and (12)) following the procedure from (Krol and Löwe, 2018), namely by applying a Gaussian smoothing and the contour filter from the Visualization Toolkit (VTK) (Schroeder et al., 2006). The snow microstructure is then enclosed in a cubic domain, with a small air padding on the sides, defining the simulated domain's outer boundaries. As detailed below, we provided special care so that this air padding does not perturb the simulation within the snow microstructure. `MeshCriteria` parameters control the meshing algorithm in CGAL: Mesh tetrahedra are regulated by the radius-edge ratio upper bound of 1.5 and circumradius upper bound of 3 voxels, and triangles in the boundary surface mesh by the lower angular bound of 25° and radius upper bound of 0.75 voxels. These mesh parameters were manually fine-tuned through visual inspection. An objective validation of all involved parameters is provided later. We save the mesh in four files listing the nodes, bulk elements, boundary elements, and header information, defining a mesh in the format of the FE software Elmer (Malinen and Råback, 2013). In addition, we computed the boundary weight on each mesh node k

$$\omega_k = \int_\Gamma \psi_k \, d\Gamma \tag{13}$$

where ψ_k is the basis function assigned to the node k, so that the sum of all boundary weights ω_k gives the area of the whole boundary surface. Saving boundary weights is substantial for the computation of the growth velocities as surface integrals over the solution of the diffusion equations. For consistency and accuracy, employing the same integration scheme that underlies the FE solution is advantageous.

https://doi.org/10.5194/egusphere-2023-1947
Preprint. Discussion started: 13 September 2023

3.2.2 FE solution

On the tetrahedral FE mesh with preserved surface, we solve Laplace equations for temperature and water vapor (Eq. (1) - (3)) employing open-source FE software Elmer (Malinen and Råback, 2013). In order to solve the equations with the proper temperature gradient across the snow microstructure, the simulations are performed in two consecutive steps. First, the heat equation over the entire domain is solved, and its result is used to estimate how a temperature gradient across the whole domain (snow microstructure together with the small air padding on the sides) translates into the snow microstructure. This allows us to compute a corrected gradient to be applied across the whole domain to match the experimental gradient in the snow. Then, the heat and water vapor diffusion are solved using the corrected temperature gradient as boundary conditions. For the computation of heat and vapor equations, we use the standard Elmer solvers `HeatSolver` and `AdvectionDiffusionSolver`, following Fourteau et al. (2021a). The equations are solved with the iterative biconjugate gradient stabilized method (BiCGSTAB; Van der Vorst, 1992) with an `ILU` preconditioner. The maximum number of iterations is set to 2000, and the convergence tolerance to 10^{-10} for the heat equation and 10^{-12} for the diffusion equation. The correct temperature gradient across the domain is applied by setting top and bottom temperatures to

$$T_{\text{top}} = T - \frac{h \cdot \nabla T}{2}, \qquad T_{\text{bottom}} = T + \frac{h \cdot \nabla T}{2}, \tag{14}$$

where T and ∇T are the experimental temperatures and temperature gradient and h is the total height of the sample.

For the vapor boundary condition, we combine the Stefan condition (Eq. (4)) by neglecting the $\rho_v v_{\mathbf{n}}$ term due to $\rho_v \ll \rho_i$, and the Gibbs-Thomson equation (Eq. (7)) to obtain a Robin boundary condition at the ice-air interface

$$D_v \mathbf{n} \cdot \nabla \rho_v = \alpha v_{\text{kin}} [\rho_v - \rho_{v,s}(1 + d_0 H)], \qquad v_{\text{kin}} \approx 140\,\text{m}\,\text{s}^{-1},\ d_0 \approx 10^{-9}\,\text{m} \tag{15}$$

Here, the equilibrium water vapor concentration is given by the Clausius-Clapeyron relation, corrected for the Gibbs-Thomson effect: (Fourteau et al., 2021a)

$$\rho_{v,s} = \frac{M}{RT} P_0 \exp\left(\frac{L}{R}\left(\frac{1}{T_0} - \frac{1}{T}(1 + d_0 H)\right)\right), \qquad \frac{m P_0}{R} \approx 1.32\,\text{kg}\,\text{K}\,\text{m}^{-3},\ \frac{L}{R} \approx 6140\,\text{K},\ T_0 \approx 273\,\text{K} \tag{16}$$

where M is the molar mass of water, R is the ideal gas constant, L is the latent heat of sublimation of ice, T_0 is the reference temperature and P_0 is the saturation pressure at T_0. In contrast to (Calonne et al., 2014b; Fourteau et al., 2021a), the curvature term $d_0 H$ is not neglected. The mean curvature on the surface mesh is obtained following (Krol and Löwe, 2018) involving the shape operator computed with the normal vector field. We compute the field of normal vectors $\mathbf{n}$ using the dedicated routine of Elmer. It was found to be more reliable than VTK computations performed on the CGAL mesh, as the latter sometimes produces areas with reversed normal vectors.

Finally, the required local interface velocity $v_{\mathbf{n}}$ is computed using the deposition and sublimation fluxes provided by the FE simulations. For this, we use the `Calculate Loads` option of Elmer that provides the quantity of water vapor f_k removed or injected at each node k of the air ice interface. Dividing by the associated boundary weight ω_k from Eq. (13) yields the deposition/sublimation flux at the ice-air interface. Thus, the velocity at node k is recovered from the simulation as

$$(v_{\mathbf{n}})_k = -\frac{f_k}{\omega_k \rho_i} \tag{17}$$

https://doi.org/10.5194/egusphere-2023-1947
Preprint. Discussion started: 13 September 2023

3.3 Post-processing and derived SSA evolution

For a given time sequence t_1, t_2, … $t_N = t$ with $t_N = N\Delta$ of available μCT images (Eqs. (11), (12)) and available FE solutions of the vapor field, the SSA is inferred from the discretized solution of Eq. (8) obtained with forward Euler method

$$s^{n+1} = s^n + 2\Delta s^n \, \overline{v_{\mathbf{n}} H}(t_n)) \tag{18}$$

where $s^n := s(t_n)$. The rates $\overline{v_{\mathbf{n}} H}(t_n)$ are calculated for each time step t_n as surface integrals from the 3D FE solution. For that, we use the VTK package and first cut off the small air padding on the sides using `vtkClipDataSet` and extracted the preserved by meshing ice-air interface. Then we employ the image analysis derived in (Krol and Löwe, 2018), where the discretized local curvature H (identical to the input used in Eq. (15)) is calculated from the shape operator. The local interface velocity $v_{\mathbf{n}}$ is deduced from the FE simulation using Eq. (17). The surface integration for the average in $\overline{v_{\mathbf{n}} H}(t_n)$ takes into account the variable element size of the triangular mesh of the ice-air interface.

3.4 Stochastic model for the discretization error

While the combination of the theoretical solution of the diffusion equation and the SSA evolution is, in principle, exact, the 4D image data processing and the derived SSA are subject to experimental and processing errors, which propagate into the modeled decrease of $s(t)$. We resort to a simple stochastic error treatment to address the impact of these errors. To this end, we write the rigorous representation of the SSA evolution from above as

$$s^{\mathrm{true}}(t) = s(0) \, \exp\left(2 \int_0^t dt' \, r^{\mathrm{true}}(t') \right) \tag{19}$$

and indicate that the true decay rate $r^{\mathrm{true}}(t') = \overline{v_{\mathbf{n}} H}$ is in general unknown and concealed by errors. In the simplest setting, one would expect that the predicted SSA can, therefore, be written as

$$s(t) = s(0) \exp\left(2 \int_0^t dt' \, r(t') \right) \tag{20}$$

where the measured rate $r(t')$ differs from the true rate by a noise term via

$$r(t) = r^{\mathrm{true}}(t') + \delta r(t) \tag{21}$$

Here, $\delta r(t)$ is an additive noise, representing uncorrelated errors (for now of unspecified origin), which affects the measurements at each time step. This implies that, on average, the computed SSA estimates are not equal to the true value s^{true} but rather to

$$s(t) = s^{\mathrm{true}}(t) \left\langle \exp\left(2 \int_0^t dt' \, \delta r(t') \right) \right\rangle \tag{22}$$

https://doi.org/10.5194/egusphere-2023-1947
Preprint. Discussion started: 13 September 2023

where $\langle \bullet \rangle$ denotes the average with respect to the additive noise. For a finite time step Δ, the discrete solution can now be written as

$$s_\Delta(t) = s^{\text{true}}(t) \left\langle \exp\left(2\Delta \sum_{i=1}^{N} \delta r(t_i) \right) \right\rangle \tag{23}$$

where the dependence on the time step Δ has been made explicit in the notation. For uncorrelated measurement errors, we assume $\delta r_i := \delta r(t_i)$ to be i.i.d. Gaussian random variables with zero mean and variance $\langle \delta r_i^2 \rangle = \sigma^2$. Since the averaged exponential in Eq. (23) is nothing but the characteristic function of δr_i, the average can be readily calculated and written as

$$s_\Delta(t) = s^{\text{true}}(t) \exp(2\Delta\sigma^2 t) \tag{24}$$

Since the truth in Eq. (24) is unknown, *absolute* errors are a priori not accessible. However, we can exploit Eq. (24) to define a *relative* error metric that quantifies the differences due to different temporal resolutions when integrating Eq. (19). To this end, we define

$$\varepsilon(\Delta, \Delta', t) := \frac{(s_\Delta(t) - s_{\Delta'}(t))^2}{s_\Delta(t)^2} \tag{25}$$

which allows us to assess the influence of using different time steps in the SSA evolution. By simplifying Eq. (25) we infer

$$\varepsilon(\Delta, \Delta', t) = [1 - \exp(2|\Delta - \Delta'|\sigma^2 t)]^2 \tag{26}$$

which relates simulated SSA differences at time t to the temporal resolution of the model and the variance of the measurement error σ.

3.5 Workflow validation: Growth of a spherical shell

We set up a complex numerical workflow that starts from a voxel image and eventually yields a growth rate $\overline{v_{\mathbf{n}} H}$ that is computed by image analysis as a volume average from the 3D results of the FE solution. In order to validate the entire workflow, we consider a test case that can be compared to an analytical solution. To this end, we employ the classical situation of the Laplace equation in a spherical shell for the vapor concentration $\rho_v(r)$ with radial coordinate r around a spherical particle with radius R with fixed vapor concentration ρ_∞ applied at the outer shell at distance R_∞. The Robin boundary conditions (Eq. (15)) are applied at the inner surface of the sphere. In this case, the growth velocity is known analytically (e.g., (Carslaw and Jaeger, 1986)), and due to spherical symmetry, the growth rate averaged over the surface is given by the value of the solution at $r = R$, via

$$\overline{v_{\mathbf{n}} H} = \frac{v_{\mathbf{n}}}{R} = \frac{D_v}{\rho_i} \frac{\rho_\infty - \rho_{v,s}}{R\left(R - \frac{R^2}{R_\infty} + \frac{D_v}{\alpha v_{\text{kin}}}\right)} \tag{27}$$

This analytical solution is compared to the numerical solution as follows. We start from a voxel image representation of the spherical shell as illustrated by the inner sphere in Fig. 1a, where the inner radius is set to $R = 21$ voxel and the outer radius set to $R_\infty = 51$ voxel with a voxel size of 18 µm. In this way, the length scales of the test case are in a similar order of magnitude

https://doi.org/10.5194/egusphere-2023-1947
Preprint. Discussion started: 13 September 2023

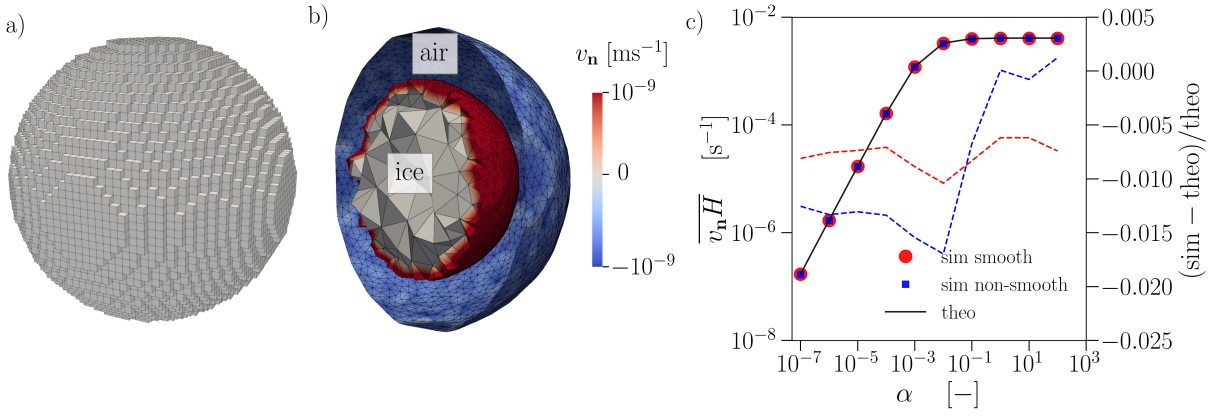

Figure 1. a) Voxeled sphere obtained from the binary image and used to constrain the problem. b) Clip of the spherical shell with visible finite elements colored by the growth velocity $v_\mathbf{n}$. c) Comparison of the theoretical (theo) and simulated (sim) solution of the spherical shell for different values of vapor attachment coefficient α.

as the real microstructures considered later. Closed triangulated inner and outer sphere surfaces are created by applying the contour filter, which is subsequently passed as input to the CGAL volume meshing. A representation of the tetrahedral volume mesh obtained from CGAL and the corresponding triangular surface meshes are shown in Fig. 1b, where the volume mesh of the air space between the sphere has been left out for visual clarity. The slightly flattened regions on the sides of the sphere due to the original representation on a cubic lattice are still visible. The figure also reveals that the obtained CGAL mesh size is adaptive, i.e., in the vicinity of the interface, element sizes are reduced. After computing the numerical solution of the Laplace equation on this geometry using Elmer, our standard post-processing procedure is used to calculate the averaged growth rate $\overline{v_\mathbf{n}H}$ as an integral over the triangulated surface of the inner sphere with local curvatures and growth velocities as described previously in Sect. 3.2.2 and 3.3. Since we shall later focus on variations as a function of the kinetic coefficient, we have repeated this procedure for ten different values of α. We also used two slightly different mesh quality parameters of the CGAL mesher to assess the sensitivity of the smoothness of the surface compared to the standard setup. The results of the validation are shown in Fig. 1c, yielding an excellent agreement of the numerical workflow with the analytical results for either smoothness. The results demonstrate that the choice of meshing and solver parameters leads to reliable numerical results. The agreement provides confidence in the correctness of the implementation of the entire workflow, which is now applied to the 4D image data of TGM.

https://doi.org/10.5194/egusphere-2023-1947
Preprint. Discussion started: 13 September 2023

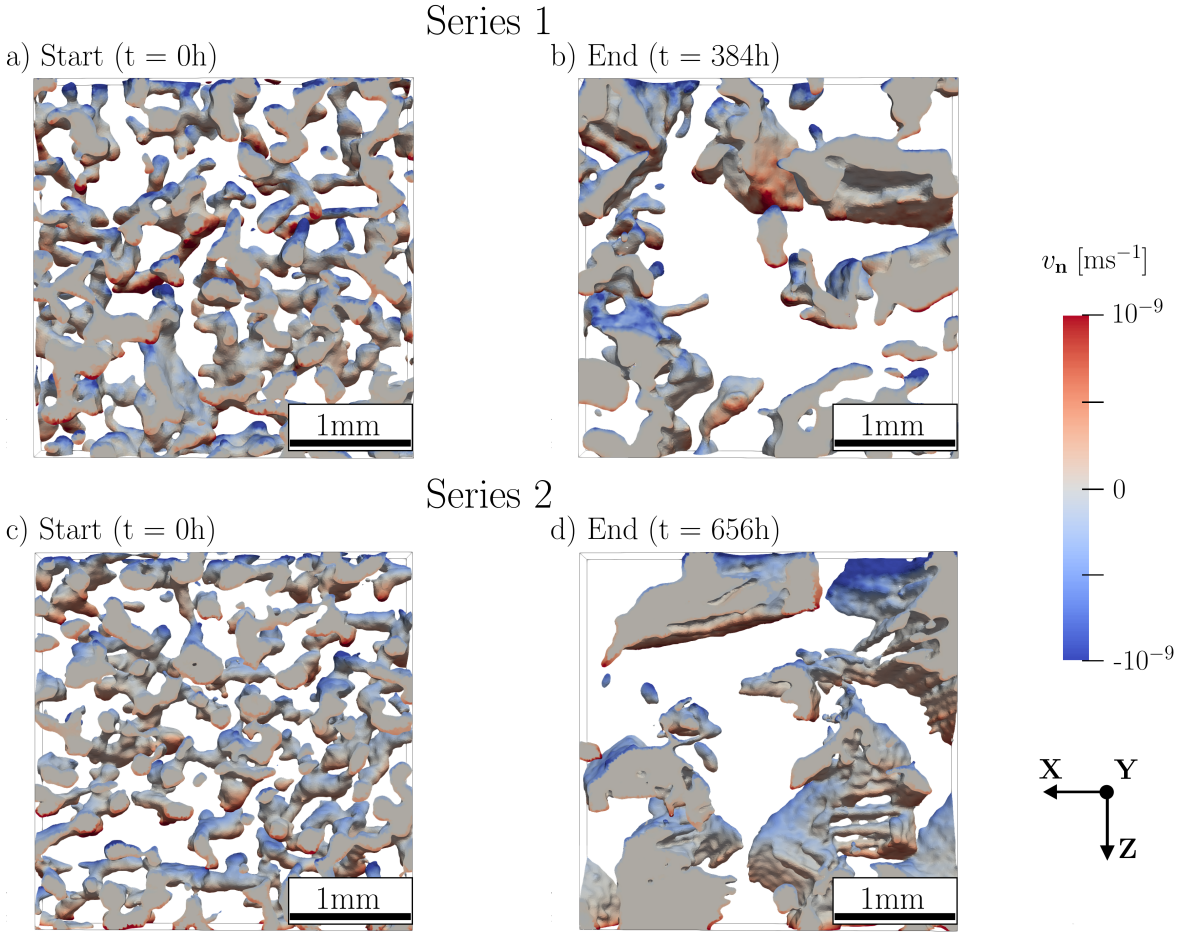

Figure 2. Evolution of the ice-air interface colored by growth velocity v_n demonstrated on cutouts of the length of 3.5 mm for a)/b) Series 1 and c)/d) Series 2.

4 Results

4.1 Overview

As an overview and for a visual inspection of the microstructures and the rates derived from the FE solution, we show in Fig. 2 the initial and the final microstructure of both experimental series, each colored by growth velocity v_n (computed using Eq. (17)). This reveals the morphological differences at the end of both experiments, where the longer experiment (Series 2) has evolved into a more pronounced depth hoar state with enhanced formation of cup crystals (Pinzer et al., 2012). The simulations from Fig. 2 were carried out for the kinetic parameter $\alpha = 10^{-1}$ for Series 1 and $\alpha = 10^{-2.25}$ for Series 2 as showing the best RMSE agreement in Fig 3c that is described in detail in the following section. As suggested by the analytical solution (Fig. 1c),

https://doi.org/10.5194/egusphere-2023-1947
Preprint. Discussion started: 13 September 2023

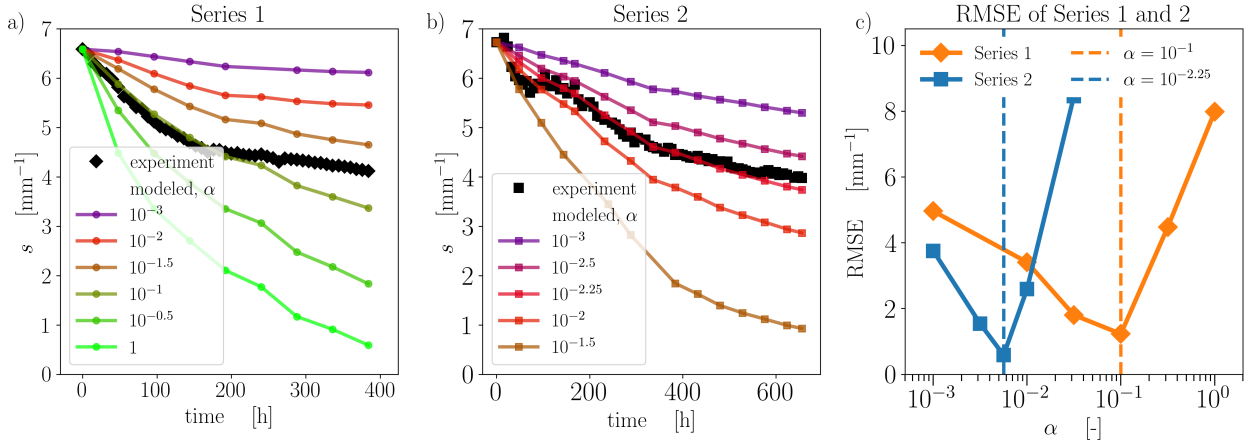

Figure 3. Time evolution of the SSA s experimental and modeled with a varying constant attachment kinetics coefficient α for a) Series 1 and b) Series 2. c) Root mean square error (RMSE) for the both series.

or the sensitivity of the vapor fluxes by (Fourteau et al., 2021a), the simulated SSA rates are highly sensitive to the kinetic coefficient.

4.2 Coarse time resolution modeling: Kinetic coefficient estimation

In the first step, we compare the temporal evolution of the SSA s between experimental data and the model using a large time step for the modeled data. This reduction in numerical effort allows us to perform a sensitivity study and estimate a value for the kinetic coefficient that best matches the experimental data. The results are shown in Fig. 3a,b. We calculate the experimental and modeled data on the same ice-air interface obtained during the numerical procedure (see Sect. 3.2 and 3.3). The temporal resolution of experimental data is refined to $\Delta \approx 8$ h, i.e. the time step of two consecutive μCT images. The modeled data are extracted with a coarse time resolution of $\Delta = 48$ h for Series 1 and $\Delta \approx 60$ h for Series 2. A fixed constant attachment kinetics coefficient α is used for each simulation. The range of α varies from 10^{-3} to 1 for Series 1 and from 10^{-3} to 10^{-1} for Series 2. The best visual agreement between the experimental and modeled data is found for $\alpha^{\text{best}}_{\text{Series 1}} = 10^{-1}$ for Series 1 and $\alpha^{\text{best}}_{\text{Series 2}} = 10^{-2.25}$ for Series 2. For Series 1, the initial stage of the modeled curve with $\alpha^{\text{best}}_{\text{Series1}}$ is close to the experimental data, while the final stage significantly underestimates the observed SSA. The same trend can be seen in Series 2, less prominent though. The experimental data of Series 2 reveals significantly more fluctuations in the initial phase, which is naturally not captured by the coarse resolution modeling.

To assess the accuracy of modeled data quantitatively, the root mean square error (RMSE) is computed according to

$$\text{RMSE} = \sqrt{\frac{\sum_{n=1}^{N} (s^n_{\text{exp}} - s^n_{\text{mod}})^2}{N}} \tag{28}$$

https://doi.org/10.5194/egusphere-2023-1947
Preprint. Discussion started: 13 September 2023

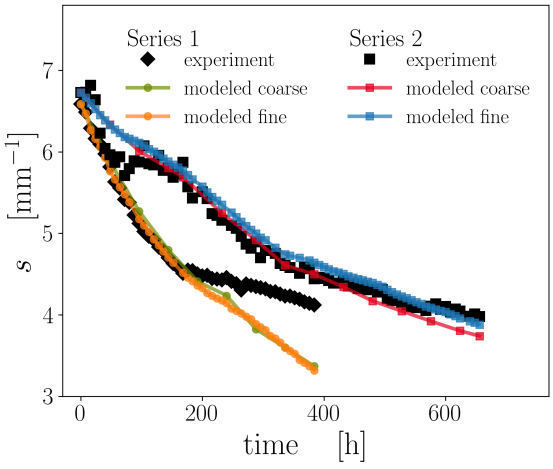

Figure 4. The time evolution of the SSA s for both series with coarse and fine temporal resolution for the best previously found values $\alpha^{\text{best}}_{\text{Series 1}}, \alpha^{\text{best}}_{\text{Series 2}}$.

where N is the number of time steps involved in the modeling. The results are shown in Fig. 3c. The minimum of the RMSE curve coincides with the best visual agreement, i.e., $\alpha^{\text{best}}_{\text{Series 1}} = 10^{-1}$, $\alpha^{\text{best}}_{\text{Series 2}} = 10^{-2.25}$. The difference between both optimal alpha values is one order of magnitude. Since the final stage of the modeled curve for Series 2 does not drop as much as for Series 1, the RMSE minimum for Series 2 is deeper despite higher data scattering.

4.3 Impact of temporal resolution

To assess the impact of temporal resolution on the modeled decrease of SSA, we performed simulations with a time step refined down the time interval between two μCT images, namely 8 h. Based on results from the previous subsection, the simulations for the fine temporal resolution are carried out for the attachment kinetic coefficients $\alpha^{\text{best}}_{\text{Series 1}}$, $\alpha^{\text{best}}_{\text{Series 2}}$ that were obtained by RMSE optimization of the coarse resolution modeling. The results are given in Fig. 4. For Series 1, the fine resolution curve essentially coincides with the coarse one. The differences are slightly enhanced for Series 2, where the fine resolution curve lies slightly above the coarse one. The good agreement between the coarse and fine resolution simulations suggests that the coarse time step used in the previous section is sufficient to estimate the optimal α values.

These modeled SSA differences due to different temporal resolutions can now be further assessed through the error metric from Eq. (25). To this end, we fix the values of α to the optimal values found in the previous section and compute the SSA evolution for various temporal resolutions. We choose different numbers of time steps N such that our model provides the time evolution of the SSA $s(t_n)$ with $n = 1, 2, \ldots N$ for different time resolutions Δ, Δ' where $\Delta = t_N/N$ (see Fig. 5a). On one hand, this allows us to calculate the error metric from Eq. (25) using the model results alone. The results are shown in Fig. 5b as solid markers for the two series. On the other hand, the error metric can also be independently estimated using the

https://doi.org/10.5194/egusphere-2023-1947
Preprint. Discussion started: 13 September 2023

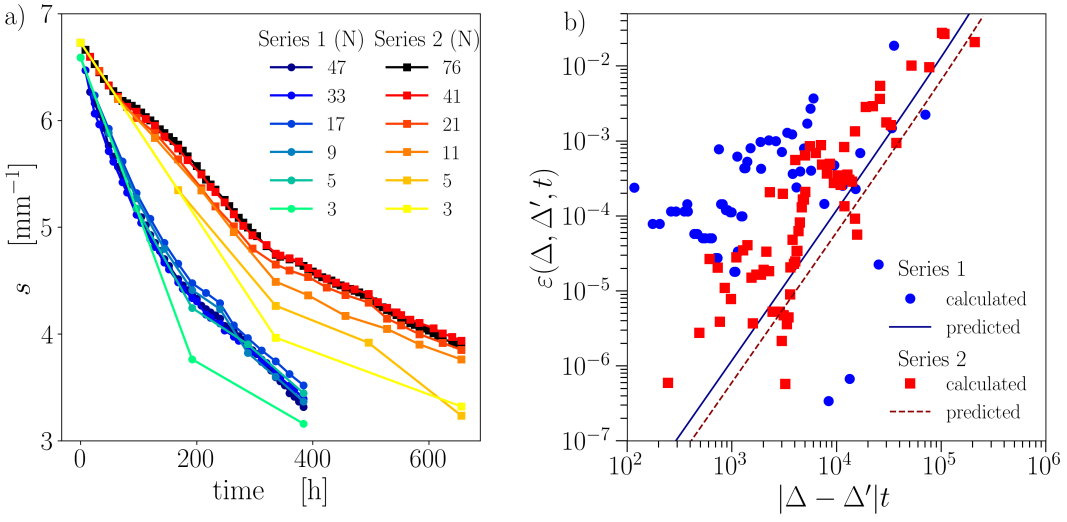

Figure 5. a) Different temporal resolutions of Series 1 and 2. b) The corresponding temporal resolution error ε calculated via Eqs. (25) and (26).

stochastic error model of Eq. (26) for the given variance σ. Fitting the variance using the least squares method on the modeled data leads to values σ_{fit} = 0.0007 and 0.0006 for Series 1 and 2, respectively, and the results are shown in Fig. 5b as lines. These values are of the same order of magnitude as the variance computed as $\dot{s}/(2s)$ from the measurements: σ_{mes} = 0.0005 and 0.0007 for Series 1 and 2, respectively. Both estimations of the impact of the temporal resolution on the error metric are in reasonable agreement. Series 2 shows a significant difference in error between the coarsest and finest time resolutions, both from simulations (red markers) or according to the μCT data (red line). On the contrary, the simulation-based estimation of Series 1 (blue markers) does not drop as much for the finest time resolutions. This comes from the fact that the modeled SSA evolution using our finest and second-finest time resolution substantially differ. Overall, the error metric's usage indicates that the time resolution's impact on the SSA evolution remains relatively small, with errors below 1%.

4.4 Signatures of a transition in kinetic coefficients during TGM

Since we obtain a good agreement between experimental and modeled data for Series 1 only in the initial stage, additional simulations were conducted to explore this further. As previously shown in (cf. Krol and Löwe, 2018, Fig. 6), the Series 1 undergoes a morphological transition at around $t \approx$160 h, where up-facing and down-facing surfaces can be morphologically distinguished by their curvature distribution. From this time on, the second moment $\overline{H^2}$ of up-facing and down-facing surfaces split up to follow a different dynamics. Such a behavior during TGM is known from other work (Calonne et al., 2014a; Granger et al., 2021) and reflects the predominant emergence of facets on down-facing surfaces while the up-facing (sublimating) surfaces remain rounded. Here, we show that this morphological transition during TGM is consistent with a transition in

https://doi.org/10.5194/egusphere-2023-1947
Preprint. Discussion started: 13 September 2023

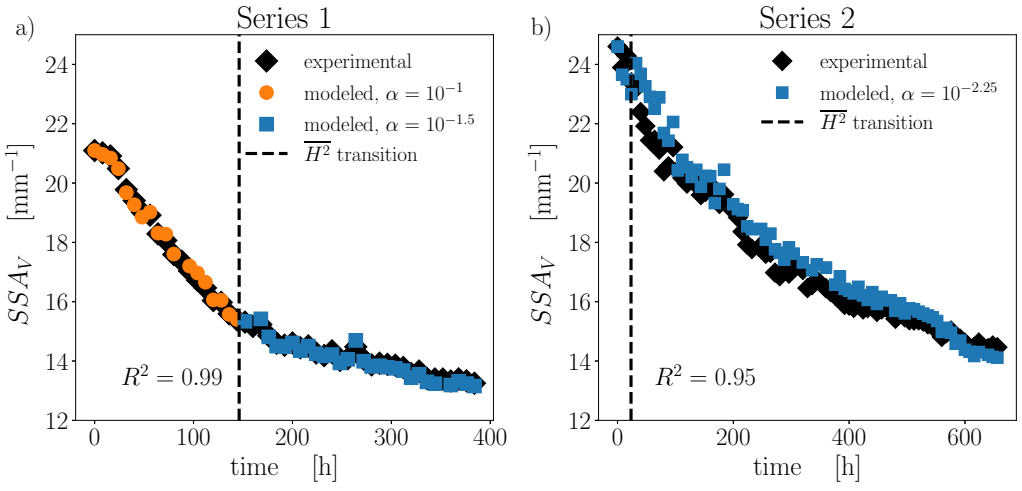

Figure 6. Comparison of experimental and modeled SSA time evolution. a) Series 1 with $\alpha^{\text{best}}_{\text{Series 1}}$ for $t \leq 160$ h and $\alpha = 10^{-1.5}$ for $t > 160$ h. b) Series 2 with $\alpha^{\text{best}}_{\text{Series 2}}$.

the overall kinetic coefficient that governs the SSA decay. To reveal the different kinetic behavior of Series 1 in the initial and final stages, we set the transition to $I(t_n), n \geq 20$, i.e. t = 160 h, and performed independent optimization of the kinetic coefficient. Very good agreement with the coefficient of determination $R^2 = 0.99$ is achieved when the kinetic coefficient is set to $\alpha = 10^{-1.5}$ for the final stage. The results for the optimal parameters are shown in Fig. 6a. While the transition is also present in Series 2 (Fig. 6 Krol and Löwe, 2018), it occurs already very early in the time series after $t \approx 24$ h, cf. Fig. 6b. This is consistent with the observation that only one value of α is sufficient to match the measured data for Series 2. Since the initial stage in Series 2 is subject to higher fluctuations, an independent optimization of another α after a few time steps is inconclusive. Overall, this leads to the slightly reduced coefficient of determination $R^2 = 0.95$ for Series 2. Fig. 6 summarizes the best possible match we obtained for the SSA in the highest resolution within the developed method.

5 Discussion

5.1 Modelling the SSA evolution from first principles

We have set up a numerical model that can simulate the evolution of one of snow's most fundamental microstructural parameters, the SSA, from 3D μCT images. The model is based on the established theoretical description of snow metamorphism through coupled vapor and heat diffusion at the pore scale (Kaempfer and Plapp, 2009; Calonne et al., 2014b). The solution of the diffusion problem thereby extends previous work characterizing TGM from μCT images (Flin and Brzoska, 2008; Pinzer et al., 2012; Krol and Löwe, 2016), where vapor fluxes were estimated only within the assumption of local equilibrium at the interface. Under this assumption, fluxes can be estimated from temperature fields and curvatures alone without explicitly

https://doi.org/10.5194/egusphere-2023-1947
Preprint. Discussion started: 13 September 2023

solving the vapor equation. Our diffusion model is essentially physically equivalent to (Kaempfer and Plapp, 2009) in the steady-state limit and has been used previously (Fourteau et al., 2021a).

The actual novelty of our work is the combination of the numerical solution of the heat and mass diffusion with the exact evolution equation for the surface area (Krol and Löwe, 2018). This combination allows us to rigorously validate the SSA dynamics without explicitly evolving the ice-air interface in 3D space. This approach is thus complementary to 4D microstructure evolution models such as (Kaempfer and Plapp, 2009) or (Bouvet et al., 2022). The advantage of including the surface area equation (Eq. (8)) into the analysis is the possibility of isolating the relevant rate term $\overline{v_{\mathbf{n}}H}$, either for constructing a stochastic error analysis (Sec. 3.4) or validation with analytical results (Sec. 3.5).

The model still requires considerable numerical resources, including volume meshing of the microstructure, the FE solution of the heat and vapor equations taking into account kinetic effects of crystal growth, the extraction of the interface velocity $v_{\mathbf{n}}$ from the vapor field and the subsequent integration of the surface area equation. As a result of the numerical effort, we were able to reproduce the decay of the SSA during TGM for the first time from "first principles", i.e. using a physical model and the actual microstructure without adjusting free parameters (in contrast to (Legagneux et al., 2004; Domine et al., 2007; Taillandier et al., 2007)). The only unknown (physical) parameter in the model is the vapor attachment coefficient, which characterizes vapor deposition and sublimation kinetics.

5.2 The kinetic coefficient

We have demonstrated that the SSA evolution in the model is highly sensitive to the kinetic coefficient (see Fig. 3). The best agreement (see Fig. 6) is obtained for values of $10^{-3} < \alpha < 10^{-1}$ (slightly different for the two time series) that fall in the intermediate range (Fourteau et al., 2021a) of possible values. This intermediate range of kinetics is neither compatible with the assumption of slow kinetics underlying the homogenization from (Calonne et al., 2014b) nor the assumption of infinitely fast kinetics, which was previously used to compute $v_{\mathbf{n}}$ from local temperature gradients (Krol and Löwe, 2016). While infinitely fast kinetics was already suggested to be inconsistent with the present experimental data sets (Krol and Löwe, 2018), this is now confirmed here from the estimated range for the values of α. From these results, we conclude that precise information about the kinetic coefficient is essential and that modeling the SSA during TGM solely using geometry and temperatures/gradients and neglecting kinetic effects (Flanner and Zender, 2006) cannot be justified.

It is well known that α is difficult to measure experimentally. This is explained in (Libbrecht, 2005) and can be easily understood from Fig. 1c: When α is commonly measured through the inversion of growth velocity $v_{\mathbf{n}}$ data, the saturation form of the curve for the growth rate $\overline{v_{\mathbf{n}}H}$ as a function of α implies significant uncertainties on α even for minor errors in the growth rate in the saturation region, where diffusion dominates. Our methodology can be considered as a new (but similar) possibility of retrieving α by comparing simulated SSA evolution curves with experimental ones. From the reasoning given above, a high uncertainty should be expected. Surprisingly, the optimization (Fig. 3) reveals a rather sharp minimum. A similar procedure for obtaining α from the comparison of measured and modeled SSA curves was recently suggested by (Bouvet et al., 2022), where a value of $\alpha \approx 9.8 \times 10^{-4}$ was obtained from a comparison of a phase field model with experimental data in isothermal metamorphism. The latter work put forward an interesting alternative route to the optimization of α from

https://doi.org/10.5194/egusphere-2023-1947
Preprint. Discussion started: 13 September 2023

experimental data by means of dimensional analysis. So, instead of conducting many simulations of different α (as done here), the same results could be obtained through non-dimensionalization and a single simulation. However, the temperature gradient case considered here is governed by two different time scales instead of only one in the isothermal case (Bouvet et al., 2022), which renders this approach less straightforward in our case. When comparing our results to other data, we see that the obtained values $10^{-1}, 10^{-1.5}$ for Series 1 and $10^{-2.25}$ for Series 2 lie in the commonly found range of $10^{-3} < \alpha < 10^{-1}$ (Libbrecht and Rickerby, 2013) which is also used by (Kaempfer and Plapp, 2009). They are slightly higher but in a similar order of magnitude as reported in (Fourteau et al., 2021a; Bouvet et al., 2022). In contrast, the kinetic coefficient from Jafari et al. (2020) translates to $\alpha \approx 5 \cdot 10^{-7}$, which is significantly below this range.

In addition to the fact that both experimental series are apparently governed by a different kinetic coefficient (Fig. 3), we have provided evidence (Fig. 6) that the kinetic coefficient may even change during a single experiment. To comprehend this finding, we recall that in snow, different parts of the ice-air interface belong to different crystallographic orientations and habits (rounded vs. faceted). Both have different attachment mechanisms and, therefore, different α (Libbrecht, 2005). Using a single, constant value of α that does not vary over the surface (as done here) must be therefore understood as an *effective* kinetic coefficient. This effective coefficient can capture actual micro-scale variations of α since still a very good agreement for the SSA (as an integral property) can be obtained. However, in principle, the assumption of a constant α in Eq. 15 must be questioned on physical grounds. On facets, one expects that α is significantly reduced by orders of magnitude with a non-linear dependence on the ambient vapor field/supersaturation (Saito, 1996). Since facets cover only a fraction of the surface, this may explain why only a moderate drop in the effective α (Fig. 6) is observed instead. Further substantiation of this hypothesis in future work is feasible even without crystal orientation measurements such as (Granger et al., 2021). The surface area evolution equation (Eq. (8)) and the pore scale diffusion model can be easily extended to deal with spatially varying kinetic coefficients on the ice-air interface and corresponding surface area sub-classes (e.g., up-facing and down-facing). Such a setup would allow us to validate the hypothesis for the kinetic coefficient transition here. Then it would be beneficial to include higher order interfacial properties like $\overline{H}$, $\overline{H^2}$ explicitly in the validation. This is, however, at the cost of evaluating higher order rate terms.

5.3 Propagation of measurement errors

Our analysis has shown why high-quality μCT data is crucial for our methodology. The complex numerical workflow contains several sources of errors that may affect the predicted SSA evolution. First, experimental input data have a limited spatial and temporal resolution, which leads to missing structural and interface correlations between two consecutive images. With a different experimental setup, such as in (Calonne et al., 2015) a higher spatial resolution may be achieved, though. Second, the volume of interest considered here for the simulations is relatively small, which explains the noisy character of the experimental parameter curves. Third, all involved image analysis and simulation procedures come with additional numerical errors. While some uncertainties can be well controlled and assessed by testing the numerical workflow against analytical solutions (see Fig. 1), the existence of remaining errors is evident.

To address these errors and their impact on SSA modeling, we have exploited that the explicit SSA representation allows us to construct a stochastic error model (Sec. 3). This model predicts how the combination of temporal resolution Δ, observation time

https://doi.org/10.5194/egusphere-2023-1947
Preprint. Discussion started: 13 September 2023

t, and methodological errors (subsumed in the variance σ of the μCT comparison data) affect the SSA prediction. The stochastic model is reasonably consistent with the observed convergence of the predictions under reduction of the time step (Fig. 5). The fact that errors can be quantitatively addressed even without knowing the true SSA is facilitated by the representation of the SSA as a differential equation (Eq. (8)). In the future, more sophisticated stochastic models should be envisaged and constructed from Eq. 8, which will further help to distinguish methodological noise and physics in the derived SSA dynamics.

5.4 Limitations and perspectives

Regarding model limitations besides the effective treatment of the kinetic coefficient approach outlined above, we have neglected the latent heat term in the interface condition for the temperature equation (Eq. 6). This leads to a slightly simpler numerical situation where heat and vapor are coupled only one way, and the heat equation can be solved in advance. Despite this simplification, we still observe that the vapor solver did not converge for a few microstructures, which explains a few missing points in the modeled time series (e.g., Fig. 6). It was previously shown (Fourteau et al., 2021b) that for low density or fast kinetics, latent heat contributes to the volume averaged heat and mass fluxes and may thus likewise enter the volume averaged rate term $\overline{v_{\mathbf{n}}H}$. This should be carefully investigated for low-density μCT time series under TGM in the future, where the numerical solution will become more demanding. In general, it would be advantageous to extend the analysis to other data sets. Here, we have used only two TGM time series which have been well studied before (Kaempfer et al., 2005; Pinzer et al., 2012; Krol and Löwe, 2018). Evaluation of high-resolution TGM experiments with systematic variations of the control parameters (microstructure, temperature, and temperature gradients) would be desirable. This would allow us to parameterize the relevant rate term $\overline{v_{\mathbf{n}}H}$ from the control parameters, which is the most promising way to proceed towards a physically based SSA equation in snow cover models.

6 Conclusions

We have addressed the SSA evolution in TGM within a rigorous framework that combines the surface area equation with pore-scale heat and mass diffusion simulations. The comparison to experimental μCT data allowed us to estimate effective kinetic coefficients that led to good agreement of the simulations with the measurements without further adjustable parameters. This shows that the evolution of SSA can be understood from the first principles of pore-scale physics (diffusive heat and mass transports), provided that the kinetic coefficient α is well-constrained. While this is a considerable step in understanding TGM our results highlight the importance of independent estimates of the kinetic coefficient in snow, which is indispensable to proceed towards physically based SSA parameterizations in snow cover models.

Code and data availability. The data will be made available through envidat.ch upon acceptance of the manuscript.

https://doi.org/10.5194/egusphere-2023-1947
Preprint. Discussion started: 13 September 2023

Author contributions. A.B. and H.L designed the study. A.B. and K.F. wrote the code. A.B. performed numerical computations. A.B, K.F. and H.L. discussed the data and wrote the manuscript. H.L. received the funding and supervised the study.

Competing interests. The authors declare having no competing interests.

Acknowledgements. A.B. and H.L. would like to thank Prof. Dr. Michael Lehning for fruitful discussions. The project was funded by the Swiss National Science Foundation (SNSF) under grant no. 200020_178831.

https://doi.org/10.5194/egusphere-2023-1947
Preprint. Discussion started: 13 September 2023

References

Adams, E. and Brown, R.: A model for crystal development in dry snow, Geophysical Research Letters, 9, 1287–1289, 1982.

Albert, M. and McGilvary, W.: Thermal effects due to air flow and vapor transport in dry snow, Journal of Glaciology, 38, 273–281, 1992.

Barrett, J. W., Garcke, H., and Nürnberg, R.: Numerical computations of faceted pattern formation in snow crystal growth, Physical Review E, 86, 011 604, 2012.

Bouvet, L., Calonne, N., Flin, F., and Geindreau, C.: Snow Equi-Temperature Metamorphism Described by a Phase-Field Model Applicable on Micro-Tomographic Images: Prediction of Microstructural and Transport Properties, Journal of Advances in Modeling Earth Systems, 14, e2022MS002 998, https://doi.org/10.1029/2022MS002998, e2022MS002998 2022MS002998, 2022.

Calonne, N., Flin, F., Geindreau, C., Lesaffre, B., and Rolland du Roscoat, S.: Study of a temperature gradient metamorphism of snow from 3-D images: time evolution of microstructures, physical properties and their associated anisotropy, The Cryosphere, 8, 2255–2274, 2014a.

Calonne, N., Geindreau, C., and Flin, F.: Macroscopic modeling for heat and water vapor transfer in dry snow by homogenization, The Journal of Physical Chemistry B, 118, 13 393–13 403, 2014b.

Calonne, N., Flin, F., Lesaffre, B., Dufour, A., Roulle, J., Puglièse, P., Philip, A., Lahoucine, F., Geindreau, C., Panel, J.-M., et al.: CellDyM: A room temperature operating cryogenic cell for the dynamic monitoring of snow metamorphism by time-lapse X-ray microtomography, Geophysical Research Letters, 42, 3911–3918, 2015.

Carslaw, H. S. and Jaeger, J. C.: Conduction of Heat in Solids, Oxford University Press, USA, 1986.

Colbeck, S.: Theory of metamorphism of dry snow, Journal of Geophysical Research: Oceans, 88, 5475–5482, 1983.

Coleou, C., Lesaffre, B., Brzoska, J.-B., Ludwig, W., and Boller, E.: Three-dimensional snow images by X-ray microtomography, Annals of glaciology, 32, 75–81, 2001.

Domine, F., Taillandier, A., Houdier, S., Parrenin, F., Simpson, W. R., and Douglas, T. A.: Interactions between snow metamorphism and climate: Physical and chemical aspects, Special Publication-Royal Society of Chemistry, 311, 27, 2006.

Domine, F., Taillandier, A.-S., and Simpson, W. R.: A parameterization of the specific surface area of seasonal snow for field use and for models of snowpack evolution, Journal of Geophysical Research: Earth Surface, 112, F02 031, https://doi.org/10.1029/2006JF000512, 2007.

Drew, D. A.: Evolution of geometric statistics, SIAM Journal on Applied Mathematics, 50, 649–666, 1990.

Dumont, M., Brun, E., Picard, G., Michou, M., Libois, Q., Petit, J., Geyer, M., Morin, S., and Josse, B.: Contribution of light-absorbing impurities in snow to Greenland's darkening since 2009, Nature Geoscience, 7, 509–512, 2014.

Flanner, M. G. and Zender, C. S.: Linking snowpack microphysics and albedo evolution, Journal of Geophysical Research: Atmospheres, 111, D12 208, 2006.

Flin, F. and Brzoska, J.-B.: The temperature-gradient metamorphism of snow: vapour diffusion model and application to tomographic images, Annals of Glaciology, 49, 17–21, 2008.

Flin, F., Brzoska, J.-B., Lesaffre, B., Coléou, C., and Pieritz, R. A.: Three-dimensional geometric measurements of snow microstructural evolution under isothermal conditions, Annals of glaciology, 38, 39–44, 2004.

Fourteau, K., Domine, F., and Hagenmuller, P.: Macroscopic water vapor diffusion is not enhanced in snow, The Cryosphere, 15, 389–406, https://doi.org/10.5194/tc-15-389-2021, 2021a.

Fourteau, K., Domine, F., and Hagenmuller, P.: Impact of water vapor diffusion and latent heat on the effective thermal conductivity of snow, The Cryosphere, 15, 2739–2755, 2021b.

https://doi.org/10.5194/egusphere-2023-1947
Preprint. Discussion started: 13 September 2023

Granger, R., Flin, F., Ludwig, W., Hammad, I., and Geindreau, C.: Orientation selective grain sublimation–deposition in snow under temperature gradient metamorphism observed with diffraction contrast tomography, The Cryosphere, 15, 4381–4398, https://doi.org/10.5194/tc-15-4381-2021, 2021.

Hagenmuller, P., Matzl, M., Chambon, G., and Schneebeli, M.: Sensitivity of snow density and specific surface area measured by microtomography to different image processing algorithms, The Cryosphere, 10, 1039–1054, https://doi.org/10.5194/tc-10-1039-2016, 2016.

Hammonds, K., Lieb-Lappen, R., Baker, I., and Wang, X.: Investigating the thermophysical properties of the ice–snow interface under a controlled temperature gradient: Part I: Experiments & Observations, Cold Regions Science and Technology, 120, 157–167, 2015.

Hanot, L. and Dominé, F.: Evolution of the Surface Area of a Snow Layer, Environmental Science & Technology, 33, 4250–4255, https://doi.org/10.1021/es9811288, 1999.

Harris Stuart, R., Faber, A.-K., Wahl, S., Hörhold, M., Kipfstuhl, S., Vasskog, K., Behrens, M., Zuhr, A. M., and Steen-Larsen, H. C.: Exploring the role of snow metamorphism on the isotopic composition of the surface snow at EastGRIP, The Cryosphere, 17, 1185–1204, https://doi.org/10.5194/tc-17-1185-2023, 2023.

Hobbs, P.: Ice Physics, Oxford Classic Texts in the Ph, OUP Oxford, 2010.

Jafari, M., Gouttevin, I., Couttet, M., Wever, N., Michel, A., Sharma, V., Rossmann, L., Maass, N., Nicolaus, M., and Lehning, M.: The Impact of Diffusive Water Vapor Transport on Snow Profiles in Deep and Shallow Snow Covers and on Sea Ice, Frontiers in Earth Science, 8, 249, https://doi.org/10.3389/feart.2020.00249, 2020.

Kaempfer, T. U. and Plapp, M.: Phase-field modeling of dry snow metamorphism, Physical Review E, 79, 031 502, 2009.

Kaempfer, T. U., Schneebeli, M., and Sokratov, S. A.: A microstructural approach to model heat transfer in snow, Geophysical Research Letters, 32, 21, https://doi.org/10.1029/2005GL023873, 2005.

Krol, Q. and Löwe, H.: Analysis of local ice crystal growth in snow, Journal of Glaciology, 62, 378–390, 2016.

Krol, Q. and Löwe, H.: Upscaling ice crystal growth dynamics in snow: Rigorous modeling and comparison to 4D X-ray tomography data, Acta Materialia, 151, 478–487, 2018.

Legagneux, L., Taillandier, A.-S., and Domine, F.: Grain growth theories and the isothermal evolution of the specific surface area of snow, Journal of applied physics, 95, 6175–6184, 2004.

Li, Y. and Baker, I.: Metamorphism observation and model of snow from summit, Greenland under both positive and negative temperature gradients in a micro computed tomography, Hydrological Processes, 36, e14 696, https://doi.org/10.1002/hyp.14696, 2022.

Libbrecht, K. G.: The physics of snow crystals, Reports on progress in physics, 68, 855, 2005.

Libbrecht, K. G. and Rickerby, M. E.: Measurements of surface attachment kinetics for faceted ice crystal growth, Journal of crystal growth, 377, 1–8, 2013.

Malinen, M. and Råback, P.: Elmer finite element solver for multiphysics and multiscale problems, Multiscale Model. Methods Appl. Mater. Sci., 19, 101–113, 2013.

Matzl, M. and Schneebeli, M.: Measuring specific surface area of snow by near-infrared photography, Journal of Glaciology, 52, 558–564, https://doi.org/10.3189/172756506781828412, 2006.

Miller, D. and Adams, E.: A microstructural dry-snow metamorphism model for kinetic crystal growth, Journal of Glaciology, 55, 1003–1011, 2009.

Picard, G., Löwe, H., and Mätzler, C.: Brief communication: A continuous formulation of microwave scattering from fresh snow to bubbly ice from first principles, The Cryosphere, 16, 3861–3866, 2022.

https://doi.org/10.5194/egusphere-2023-1947
Preprint. Discussion started: 13 September 2023

Pinzer, B. and Schneebeli, M.: Breeding snow: an instrumented sample holder for simultaneous tomographic and thermal studies, Measurement Science and Technology, 20, 095 705, 2009a.

Pinzer, B. R. and Schneebeli, M.: Snow metamorphism under alternating temperature gradients: Morphology and recrystallization in surface snow, Geophysical Research Letters, 36, 23, https://doi.org/10.1029/2009GL039618, 2009b.

Pinzer, B. R., Schneebeli, M., and Kaempfer, T. U.: Vapor flux and recrystallization during dry snow metamorphism under a steady temperature gradient as observed by time-lapse micro-tomography, The Cryosphere, 6, 1141–1155, https://doi.org/10.5194/tc-6-1141-2012, 2012.

Pokrifka, G. F., Moyle, A. M., Hanson, L. E., and Harrington, J. Y.: Estimating Surface Attachment Kinetic and Growth Transition Influences on Vapor-Grown Ice Crystals, Journal of the Atmospheric Sciences, 77, 2393 – 2410, https://doi.org/10.1175/JAS-D-19-0303.1, 2020.

Saito, Y.: Statistical physics of crystal growth, World Scientific, 1996.

Schleef, S. and Loewe, H.: X-ray microtomography analysis of isothermal densification of new snow under external mechanical stress, Journal of Glaciology, 59, 233–243, 2013.

Schneebeli, M. and Sokratov, S. A.: Tomography of temperature gradient metamorphism of snow and associated changes in heat conductivity, Hydrological Processes, 18, 3655–3665, 2004.

Schroeder, W., Martin, K., and Lorensen, B.: The visualization toolkit, 4th edn. Kitware, New York, 2006.

Schweizer, J., Bruce Jamieson, J., and Schneebeli, M.: Snow avalanche formation, Reviews of Geophysics, 41, 4, 2003.

Shreve, R.: Migration of air bubbles, vapor figures, and brine pockers in ice under a temperature gradient, Journal of Geophysical Research, 72, 4093–4100, 1967.

Taillandier, A.-S., Domine, F., Simpson, W. R., Sturm, M., and Douglas, T. A.: Rate of decrease of the specific surface area of dry snow: Isothermal and temperature gradient conditions, Journal of Geophysical Research: Earth Surface, 112, F3, 2007.

The CGAL Project: CGAL User and Reference Manual, CGAL Editorial Board, 5.5.1 edn., https://doc.cgal.org/5.5.1/Manual/packages.html, 2022.

Van der Vorst, H. A.: Bi-CGSTAB: A fast and smoothly converging variant of Bi-CG for the solution of nonsymmetric linear systems, SIAM Journal on scientific and Statistical Computing, 13, 631–644, 1992.

Wang, X. and Baker, I.: Evolution of the specific surface area of snow during high-temperature gradient metamorphism, Journal of Geophysical Research: Atmospheres, 119, 13–690, 2014.

Wiese, M. and Schneebeli, M.: Snowbreeder 5: a Micro-CT device for measuring the snow-microstructure evolution under the simultaneous influence of a temperature gradient and compaction, Journal of Glaciology, 63, 355–360, 2017.

Zermatten, E., Schneebeli, M., Arakawa, H., and Steinfeld, A.: Tomography-based determination of porosity, specific area and permeability of snow and comparison with measurements, Cold Regions Science and Technology, 97, 33–40, https://doi.org/10.1016/j.coldregions.2013.09.013, 2014.